

Hard X-ray spectrum of the Vela pulsar and its wind nebula constrained by NuSTAR

OLEG KARGALTSEV,¹ JEREMY HARE,^{2,3,4} AND ALEXANDER LANGE^{1,5}

¹*Department of Physics, The George Washington University, 725 21st St. NW, Washington, DC 20052*

²*Astrophysics Science Division, NASA Goddard Space Flight Center, 8800 Greenbelt Rd, Greenbelt, MD 20771, USA*

³*Center for Research and Exploration in Space Science and Technology, NASA/GSFC, Greenbelt, Maryland 20771, USA*

⁴*The Catholic University of America, 620 Michigan Ave., N.E. Washington, DC 20064, USA*

⁵*Department of Space Physics, University of Maryland Baltimore County, Baltimore, MD 21250, USA*

ABSTRACT

We present the analysis of 200-ks NuSTAR observation of the Vela pulsar and the pulsar wind nebula (PWN). The phase-resolved spectra corresponding to two main peaks in the folded pulse profile differ significantly. The spectrum of Peak 1 is significantly harder than that of Peak 2 in qualitative agreement with the earlier RXTE results. However, for both spectra, the values of power-law (PL) fit photon indices, Γ , are noticeably larger than the previously reported values. The harder (Peak 1) spectrum has $\Gamma = 1.10 \pm 0.15$ which is close to those measured for the bright inner jets of the PWN. We used the off-pulse interval to remove the emission from the pulsar and measure the compact pulsar wind nebula (PWN) spectrum in hard X-rays. We also measured the spectrum from the south-western (SW) region of the PWN which is resolved by NuSTAR from the compact PWN. For both regions, we fit the NuSTAR spectra by themselves and together with the Chandra X-ray Observatory spectra. We found that the PWN spectrum (for both regions) requires a more complex model than a simple PL. The fits to compact PWN spectrum favor exponentially cutoff PL model, with $E_c \approx 50$ keV over the broken PL model. The observed synchrotron photon energies imply electrons accelerated to ≈ 150 TeV.

1. INTRODUCTION

The Vela pulsar (PSR 0833-45), lying at a distance of ≈ 290 pc (Dodson et al. 2003), is the youngest of the few nearby pulsars and has been studied extensively across the electromagnetic spectrum (see e.g., Romani et al. 2005 and references therein). Spinning with a period of 89 ms, Vela is the brightest GeV pulsar in the γ -ray sky. The pulsar's spectrum is dominated by non-thermal emission everywhere but in soft X-rays where thermal emission from the neutron star (NS) surface prevails (Pavlov et al. 2001). Outside the soft X-ray energy range (Sanwal et al. 2002) the phase-integrated multiwavelength spectrum is complex showing multiple breaks (see e.g., Danilenko et al. 2011). The multi-wavelength pulse profiles are similarly complex with 5-6 discernible peaks throughout the 89-ms pulse period whose relative strengths vary with energy (see Figure 5 of Spolon et al. 2019). These changes are noticeable even across the 2-30 keV energy range explored with the Rossi X-ray Timing Explorer (RXTE; Strickman et al. 1999; Harding et al. 2002; Kuiper & Hermsen 2015). By performing phase-resolved analysis of RXTE data Harding et al. (2002) found that the peak's spectra can be described by power-law model with photon indices, Γ ranging from 0.8 to 2.1. The lowest value of Γ indicates a very hard spectrum implying a very unusual particle

spectral energy distribution (SED) assuming the standard synchrotron emission mechanism. This spectrum is also harder than the spectrum of the hardest parts of the pulsar wind nebula (PWN), $\Gamma \approx 1.2$ (Kargaltsev & Pavlov 2004; Kargaltsev et al. 2017).

Owing to its young age¹. (≈ 11 kyrs) and relatively high spin-down power ($\dot{E} = 7 \times 10^{36}$ erg s⁻¹), the pulsar inflates a bubble filled with energetic particles within the Vela supernova remnant (SNR) interior (Bock et al. 1998; Dodson et al. 2003). The compact axisymmetric PWN exhibits a complex fine structure (both spatial and spectral) resolved in the Chandra X-ray Observatory (CXO) images (Pavlov et al. 2001; Helfand et al. 2001; Pavlov et al. 2003; Durant et al. 2013). The PWN spectral maps, obtained from CXO data in the 0.5-8 keV range, show one of the hardest X-ray spectra among all known PWNe (Kargaltsev et al. 2017). Studying the spectral changes with distance from the pulsar constrains particle transport mechanisms and the evolution of the particle SED due to radiative cooling (see, e.g., Porth et al. 2016). Previous observations in hard X-

¹ The age of 11 kyr is based on the standard assumption of a braking index of 3. The actual Vela pulsar age may be somewhat larger (see, e.g., Espinoza et al. 2017)

rays lacked the angular resolution provided by NuSTAR (Mattana et al. 2011), making it difficult to isolate the PWN’s contribution from the pulsar and to accurately subtract the local background. The recent IXPE measurements found a very high degree of polarization (up to 60%) for the compact PWN, suggesting the electrons in the PWN are accelerated with little or no turbulence in a highly uniform toroidal magnetic field (Xie et al. 2022).

On larger angular scales the PWN is asymmetric, extending much further away from the pulsar in the SW direction compared to the north-eastern (NE) side. Unfortunately, IXPE does not provide polarization measurements outside the bright compact PWN but radio data still suggest that the magnetic field is highly regular and the polarization fraction remains high (Dodson et al. 2003). The SW extension of the compact PWN connects smoothly to the so-called “cocoon” (a possible relic PWN), whose soft X-ray spectrum, measured with XMM-Newton, appears to be a mixture of thermal and non-thermal emission (Slane et al. 2018). The cocoon is also detected at TeV energies with the High Energy Stereoscopic System (H.E.S.S.; H. E. S. S. Collaboration et al. 2019).

We obtained NuSTAR observation of the Vela PWN to extend the spectral coverage out to 70 keV for the compact PWN, to separate the pulsed emission from that of the PWN using photon phases, and to spatially resolve the spectrum of the SE part of the PWN from that of the compact PWN. We also made use of Fermi Large Area Telescope (LAT) data to determine pulsar’s spin period and its spin period derivative and to compare γ -ray and hard X-ray pulse profiles. In Section 2 we describe the data used in this paper while Sections 3 and 4 report the results of timing and spectral analysis, respectively. The discussion of the results follows in Section 5. We conclude with the summary in Section 6.

2. OBSERVATIONS

2.1. NuSTAR

NuSTAR (Harrison et al. 2013) observed the Vela pulsar region on 2021 March 21 (ObsID 30601032002; start time MJD 59294.66253502, stop time MJD 59298.99801064) with a total scientific exposure of 205,080 seconds. We reprocessed the data using HEASoft v6.29 and NuSTAR CALDB v20210427. We ran the standard `nupipeline` tool, which applied all the latest calibrations and filtering. We also barycenter-corrected the photon arrival times originating from the pulsar’s position, using NuSTAR clock correction file 20100101v125 which also corrects for NuSTAR’s clock drift, providing a timing accuracy of $\sim 65 \mu\text{s}$

(Bachetti et al. 2021). We excluded times of high particle background² using the options `saacalc=2`, `saamode=optimized`, and `tentacle=no`, which had a minimal impact on the total exposure time ($< 0.2\%$). We extracted spectra using `nuproducts` (with option `extended=yes` for analysis of the PWN).

2.2. Chandra X-ray Observatory

We also used archival CXO ACIS imaging data (from 3 observations obtained between Aug 15 2010 and Sep 4 2010; ObsIDs 12073, 12074, and 12075; total scientific exposure 121 ks) to improve the statistics and to extend the data analysis to lower energies for the PWN spectra. The data reduction and fits followed standard procedures described in the CIAO analysis threads³. Since all three CXO observations are taken close to each other and the target was placed at the same location on ACIS-S3 chip, we chose to combine⁴ spectra and responses for all observations to simplify the subsequent analysis steps. However, we also verified that including all 3 CXO spectra individually produces similar results. For our analysis, we used CIAO 4.13 and CALDB 4.9.4.

2.3. Fermi LAT

More than 13 years of Fermi LAT data were collected and used to analyze the high-energy emission from the Vela pulsar. We used `gtselect` from *FermiTools*⁵ to extract data from a 1° radius region of interest centered on Vela pulsar. Additionally, we applied a selection on the times and energies, filtering our dataset to match the Fermi LAT ephemeris range (valid between MJD 54682.71577-59500.98129) and limiting photon energies to be between 0.3 GeV to 6 GeV. Barycentric corrections were made with PINT’s software (Luo et al. 2021). We used the JPL DE421 planetary ephemeris for all timing analyses.

3. TIMING

We performed Z_n^2 test (Buccheri et al. 1983; for $n=5$, given the multi-peak nature of the hard X-ray pulse profile; Harding et al. 2002) on the NuSTAR data, using a 2D grid of frequency (f) and frequency derivative (\dot{f}). We also varied the circular extraction aperture radius, to maximize the pulsar contribution, and found that the

² See https://nustarsoc.caltech.edu/NuSTAR_Public/NuSTAROperationSite/SAA_Filtering/nulyses_reports/30601032002/nu30601032002_SAA_Report_A.pdf

³ <https://cxc.cfa.harvard.edu/ciao/threads/>

⁴ Following the recipe provided at <https://cxc.cfa.harvard.edu/ciao/threads/coadding/>

⁵ <https://fermi.gsfc.nasa.gov/ssc/data/analysis/software/>

Z_5^2 values grow up to $r = 50''$ and then level off. In addition, we explored the dependence of Z_5^2 on the energy range and found that it is maximized when the full range (3-79 keV) is used. Figure 1 shows the expected f and \dot{f} calculated using the *PINT* timing software with the Vela Fermi LAT ephemeris⁶ based on 13.2 years of data (courtesy of Mathew Kerr). Figure 1 shows that the prediction of f and \dot{f} from NuSTAR timing agrees with that based on the Fermi LAT ephemeris.

To produce the NuSTAR pulse profiles we adopted two different approaches. In the first approach, we assigned phases to all NuSTAR photons extracted from the $r = 50''$ aperture (in 3-79 keV band), as well as the Fermi-LAT photons (in 0.3-6 GeV band), using *PINT*'s *photonphase* and *fermiphase* respectively. This approach ensures that the NuSTAR and LAT profiles are co-aligned (Figure 2) and shows that the two main peaks, dubbed Peak 1 (Pk1) and Peak 2 (Pk2), seen in the NuSTAR data coincide with the peaks seen in the Fermi LAT pulse profiles. In the other approach, we used the f and \dot{f} values obtained⁷ from the Z_5^2 test to fold the NuSTAR pulse profile. As one can see from Figure 2 there are small differences between the two NuSTAR profiles (first and second panels from the top) but overall they are quite similar. The corresponding pulsed fractions (defined as the ratio of the area above the minimum to the total area under the pulse profile) are $4.0\% \pm 1.1\%$ and $4.5\% \pm 1.1\%$, respectively. In the same figure we also plot pulse profiles in 3-10 and 10-79 keV. They are fairly similar with Pk2 becoming broader and less pronounced in 10-79 keV, in agreement with its softer spectrum (see Section 4.1).

4. SPECTRA

In this section we describe spectral fitting performed with XSPEC package version 12.13.1 (Arnaud 1996).

4.1. Pulsar

Since the PWN photons strongly dominate those from the pulsar within the chosen $50''$ aperture centered on the pulsar, we only fit the pulsar spectrum extracted for the two phase bins corresponding to Pk1 and Pk2 in the γ -ray pulse profile (see Figure 3 and Table 1). Since the intervening hydrogen column is small ($\sim 3 \times 10^{20} \text{ cm}^{-2}$), and NuSTAR observes at energies $> 3 \text{ keV}$, we simply ignore the foreground absorption. The PWN emission strongly dominates the pulsed emission, so to account

⁶ The ephemeris validity range MJD 54682.71577-59500.98129 includes the NuSTAR observation interval.

⁷ for the middle of the NuSTAR observation (59296.84506887 MJD).

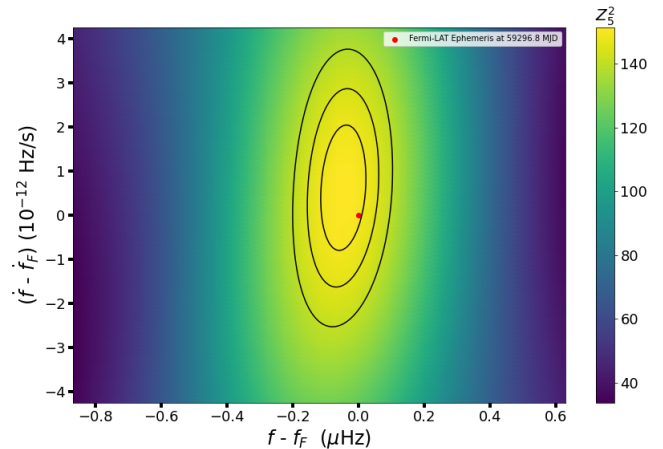


Figure 1. Z_5^2 distribution as a function of frequency and its derivative for NuSTAR data. Zero (shown by a red point) corresponds to $f = f_F = 11.18437086731769 \text{ Hz}$ and $\dot{f} = \dot{f}_F = -1.52431976409 \times 10^{-11} \text{ Hz s}^{-1}$ inferred from the Fermi LAT ephemeris for the middle of NuSTAR observation (MJD 59296.83198754). The black lines show 1, 2 and 3 σ confidence contours (see Buccheri et al. 1983 and Appendix A in Posselt et al. 2024).

for it when fitting the spectra of the peaks, we first fit the spectra of the Off-Pulse (OP) interval ($\phi = 0.74 - 0.80$) with a power-law. We then fit the Pk1 ($\phi = 0.18 - 0.22$) and Pk2 ($\phi = 0.52 - 0.68$) spectra with two PLs, where for the first PL the photon index and normalization are frozen to their best-fit values from the fit to OP spectra while for the second PL (representing the Pk1 or Pk2 spectra) both parameters are fitted. We find the Pk1 spectrum with $\Gamma_1 = 1.07 \pm 0.15$ to be substantially harder than the Pk2 spectrum with $\Gamma_2 = 1.62 \pm 0.20$. The uncertainties are given at the 68% confidence level for a single interesting parameter. The PL fit quality is good with $\chi^2/\text{d.o.f.} \approx 0.90$ and 1.16) and for Pk1 and Pk2 spectra, respectively.

4.2. PWN: NuSTAR

In order to explore the PWN spectrum we define two regions, one for the compact PWN and one for the SE extension (white and green circles in Figure 4, respectively). The results of the fits are summarized in Table 2. The extracted spectra are binned to ≥ 200 photons per bin. In both cases the background spectrum is extracted from the $r = 40''$ circle located west of the pulsar, on the same chip as PWN, centered at R.A.=8h34m54s, Decl.= $-45^\circ 12' 04''$ (see Figure 4). During the spectral fits the background spectrum is subtracted from that of the source after being binned the same way. We first fit NuSTAR-only spectra (in 3-79 keV range). The photon indices are tied for FPMA and FPMB detector spectra but their normalizations are left free.

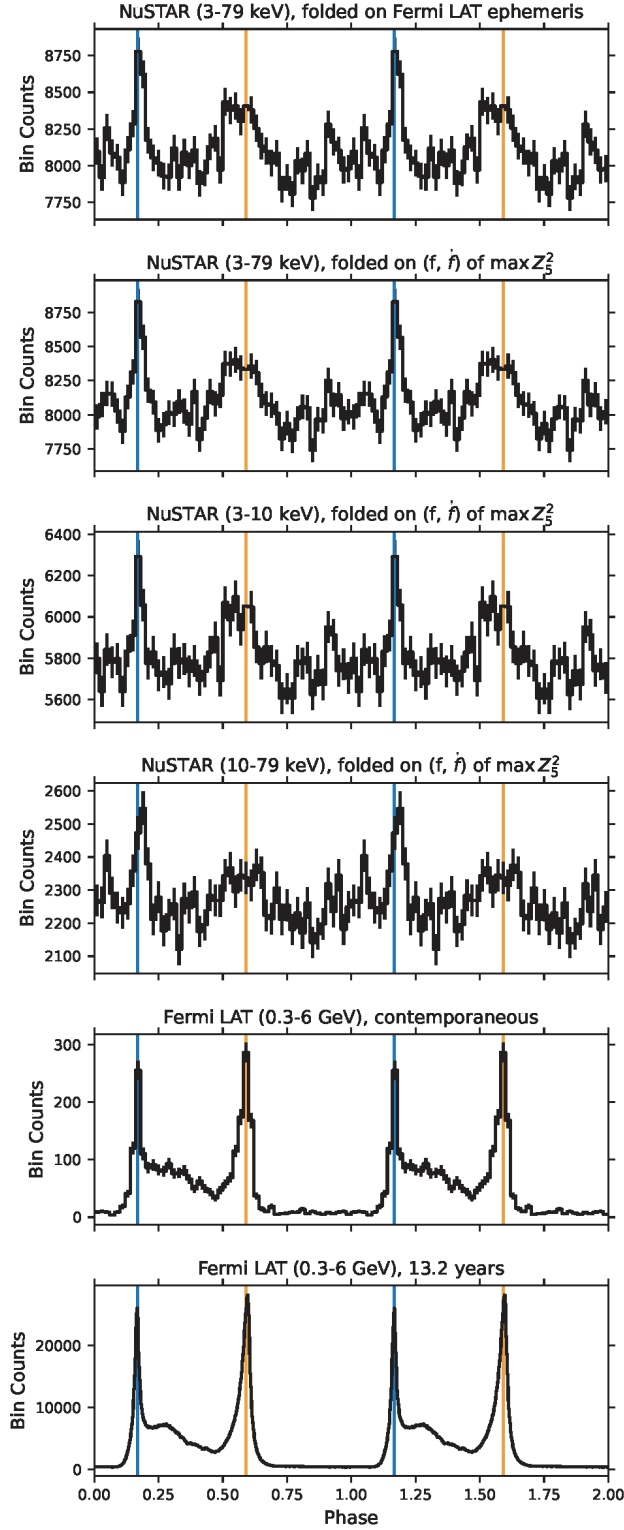


Figure 2. NuSTAR and Fermi LAT pulse profiles. Each pulse NuSTAR profile consists of 50 equal-width phase bins. The blue and orange vertical lines correspond to the phase of Peak 1 (Pk1) and Peak 2 (Pk2) as determined from the plot in the bottom panel. See Section 3 for details. The epoch of zero phase is 56623.15526604 MJD.

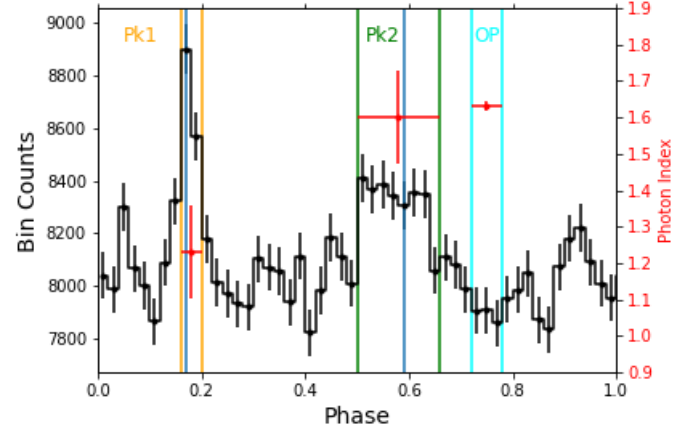


Figure 3. The black line and errorbars show the 3-79 keV NuSTAR pulse profile of Vela pulsar with the 3 phase intervals used for the phase-resolved analysis shown (orange - Pk1; green - Pk2, blue - OP). The dark blue vertical lines show the phases of the two peaks in the Fermi LAT pulse profile. The red errorbars show the photon index measurements (on the right vertical axis) for the corresponding phase intervals. See also Table 1 and text for details.

For the compact PWN region ($r = 50''$ circle centered on the pulsar) we only use off-pulse (OP) photons to avoid contamination by the pulsar (99% of photons are expected to come from the PWN). The spectrum contains 9,661 (FPMA) and 10,557 (FPMB) photons in 3-79 keV. The background contribution is negligible. The best-fit with a simple PL model gives $\Gamma = 1.64 \pm 0.01$ but the fit quality is poor with $\chi^2 = 141$ for 91 d.o.f. Also, some systematic large-scale residuals at low and high energies of the energy range are present. We, therefore, tried to also fit a broken PL model (“bknpower” in XSPEC; hereafter BPL) and obtained $\Gamma_1 = 1.57 \pm 0.02$, break energy $E_b = 10.9 \pm 1.5$ keV and $\Gamma_2 = 1.79 \pm 0.05$ with a noticeable improvement in large-scale residuals resulting in $\chi^2 = 128$ for 89 d.o.f. An exponentially cutoff PL (“cutoffpl” in XSPEC; hereafter ECPL) model fits equally well ($\chi^2 = 122$ for 91 d.o.f.) with $\Gamma = 1.50 \pm 0.04$ and a rather uncertain exponential cut-off energy $E_c = 79^{+26}_{-16}$ keV.

The spectrum from SW extension region (see Figure 4, bottom) has 17,059 and 16,380 photons in FPMA and FPMB, respectively, with 80% coming from the source for either of the detectors. The PL fit quality is good with $\Gamma = 1.81 \pm 0.02$ with $\chi^2 = 232$ for 241 d.o.f. There are no significant systematic residuals. Therefore, we have not attempted any fits with more complex models.

4.3. PWN: NuSTAR+CXO

We now perform the joint fits to the NuSTAR and CXO ACIS spectra for the same as above two PWN

regions. For CXO observations the background is taken from a source-free circular region with $r = 1'$ located north of the pulsar and centered at R.A.=8h35m18s and Decl.=−45°07'10". We jointly fit spectra in 1-79 keV range with the CXO ACIS spectrum extending up to 5 keV and NuSTAR spectrum starting from 3 keV. We also excluded a narrow 1.9-2.3 keV region from the CXO spectrum because it seems to show local residuals which could be instrumental⁸. All spectra are binned to have at least 200 counts per bin. For both CXO and NuSTAR the background spectrum is subtracted from the source's spectrum. In these fits we used models modified by ISM absorption modeled with XSPEC's "tbabs" using *wilm* abundances (Wilms et al. 2000) with fixed $n_H = 3.2 \times 10^{20} \text{ cm}^{-2}$ (see Pavlov et al. 2001). The normalizations of different detectors/instruments (FPMA, FPMB, and ACIS) are allowed to vary independently while the rest of the fitting parameters are tied.

For the SW extension PWN region (polygon in Figure 4), the joint spectra and the best fits are shown in Figure 5, left panels. To avoid contamination by the compact PWN, the polygon boundary is at least 150" away from the pulsar and $\approx 100''$ away from the bright compact PWN structure (arcs and jets) (seen in the CXO image). Although the single PL fit quality is acceptable, with $\Gamma = 1.81 \pm 0.02$, there is a noticeable large-scale structure in the residuals. Both BPL and ECPL models are providing good fits. For the former, $\Gamma_1 = 1.64^{+0.03}_{-0.05}$, break energy $E_b = 3.0^{+0.4}_{-0.7} \text{ keV}$ and $\Gamma_2 = 1.82 \pm 0.02$. The low energy of the break could explain why the BPL model was not required when only NuSTAR data were fitted in the 3-79 keV range. On the other hand, the coincidence between the E_b and the start of NuSTAR energy range indicate that the improvement associated with the broken PL may come from imperfection in calibration (see also Madsen et al. 2017). If the latter is indeed the case then one can expect a similar situation with spectral fits for the compact PWN region. The ECPL model fits the spectrum nearly equally well with $\Gamma = 1.64 \pm 0.02$ and $E_c = 50^{+14}_{-9} \text{ keV}$.

For the compact PWN region the CXO and NuSTAR spectra and the joint fits are shown in the right panels of Figure 5. For the ACIS spectrum, also extracted from $r = 50''$ region centered on the pulsar, we exclude the $r = 3''$ region centered on the pulsar. We use the OP phase interval for NuSTAR data in or-

Table 1. Phase-resolved spectral fitting results.

Feature name	Phase range	Γ
Narrow peak small (Pk1)	0.16-0.20	1.06 ± 0.16
Broad peak (Pk2)	0.50-0.66	1.62 ± 0.20
Background (OP interval)	0.72-0.78	1.65 ± 0.01

der to exclude the pulsar. The simple absorbed PL fit is clearly not satisfactory (see Figure 5). While the BPL fit is better ($\chi^2=526$ for 458 d.o.f.), it does show systematic residuals at high energies with the model over predicting the data. The best-fit parameters are $\Gamma_1 = 1.46 \pm 0.01$, break energy $E_b = 2.7 \pm 0.1 \text{ keV}$ and $\Gamma_2 = 1.60 \pm 0.01$. The break energy is again close to the lower energy end of NuSTAR range which may hint at a possible cross-calibration issue. The above-mentioned high-energy residuals disappear when the broken PL model is replaced with the ECPL model ($\chi^2 = 537$ for 459 d.o.f.) with best-fit $\Gamma = 1.459 \pm 0.005$ and the cut-off energy of $E_c = 50 \pm 4 \text{ keV}$. However, the positive residuals between 2 and 3 keV become more noticeable. This could again be an indication of imperfect cross-calibration which is more noticeable for the bright compact PWN due to the much larger number of photons in the ACIS spectrum.

5. DISCUSSION

5.1. Pulsar

The NuSTAR pulse profile of Vela pulsar is remarkably complex in 3-79 keV range with multiple narrow peaks of which two align with the two main peaks (Pk1 and Pk2) seen in the LAT pulse profile (see Figure 2). However, while in the LAT pulse profile Pk1 and Pk2 are both very sharp, the hard X-ray counterpart of Pk2 is much broader than that of Pk1. The 3-79 keV NuSTAR pulse profile overall looks similar to the one obtained from RXTE PCA (Proportional Counter Array) data in 8-24 keV range more than two decades ago. In particular, the four most pronounced peaks (two main peaks Pk1 and Pk2, and 2 smaller ones preceding Pk1) are easily identifiable in both NuSTAR and RXTE pulse profiles (see Figure 4 of Kuiper & Hermsen 2015). We note that, while we find a modest evolution in the pulse shape between the 3-10 and 10-79 keV energy ranges (Figure 2), the RXTE pulse shape appears to evolve more substantially between 4-8 and 8-24 keV (e.g., relative amplitudes of Pk1 and Pk2 change noticeably; see Figure 4 in Kuiper & Hermsen 2015). While we are not exactly sure about the reason of the apparent discrepancies, they may originate from different dependencies

⁸ The residuals are stronger in two out of 3 CXO observations. They become noticeable only with a very large number of photons in the fit to the compact PWN region and are only marginally seen in the fit for the SW extension. However, for consistency, we excluded the same energy range in both spectra.

Region	Model	Mission(s)	Γ or Γ_1	E_c or E_b (keV)	Γ_2	χ^2	d.o.f.
Comp. PWN	PL	NuSTAR	1.64 ± 0.01	—	—	141	91
Comp. PWN	ECPL	NuSTAR	1.50 ± 0.04	79^{+26}_{-16}	—	128	90
Comp. PWN	BPL	NuSTAR	1.57 ± 0.02	10.9 ± 0.5	1.79 ± 0.05	122	89
Comp. PWN	PL	NuSTAR+CXO	1.509 ± 0.002	—	—	733	460
Comp. PWN	ECPL	NuSTAR+CXO	1.459 ± 0.005	50 ± 4	—	537	459
Comp. PWN	BPL	NuSTAR+CXO	1.46 ± 0.01	2.7 ± 0.1	1.60 ± 0.01	526	458
SW PWN	PL	NuSTAR	1.81 ± 0.02	—	—	232	241
SW PWN	PL	NuSTAR+CXO	1.73 ± 0.01	—	—	413	370
SW PWN	ECPL	NuSTAR+CXO	1.64 ± 0.02	50^{+14}_{-9}	—	391	369
SW PWN	BPL	NuSTAR+CXO	$1.64^{+0.03}_{-0.05}$	$3.0^{+0.4}_{-0.7}$	1.82 ± 0.02	389	368

Table 2. Spectral fits with 3 different models for compact and SW PWN regions. See text for details. The uncertainties are given at the 68% confidence level for a single interesting parameter. For the CXO+NuSTAR fits we fixed n_H at $3.2 \times 10^{20} \text{ cm}^{-2}$.

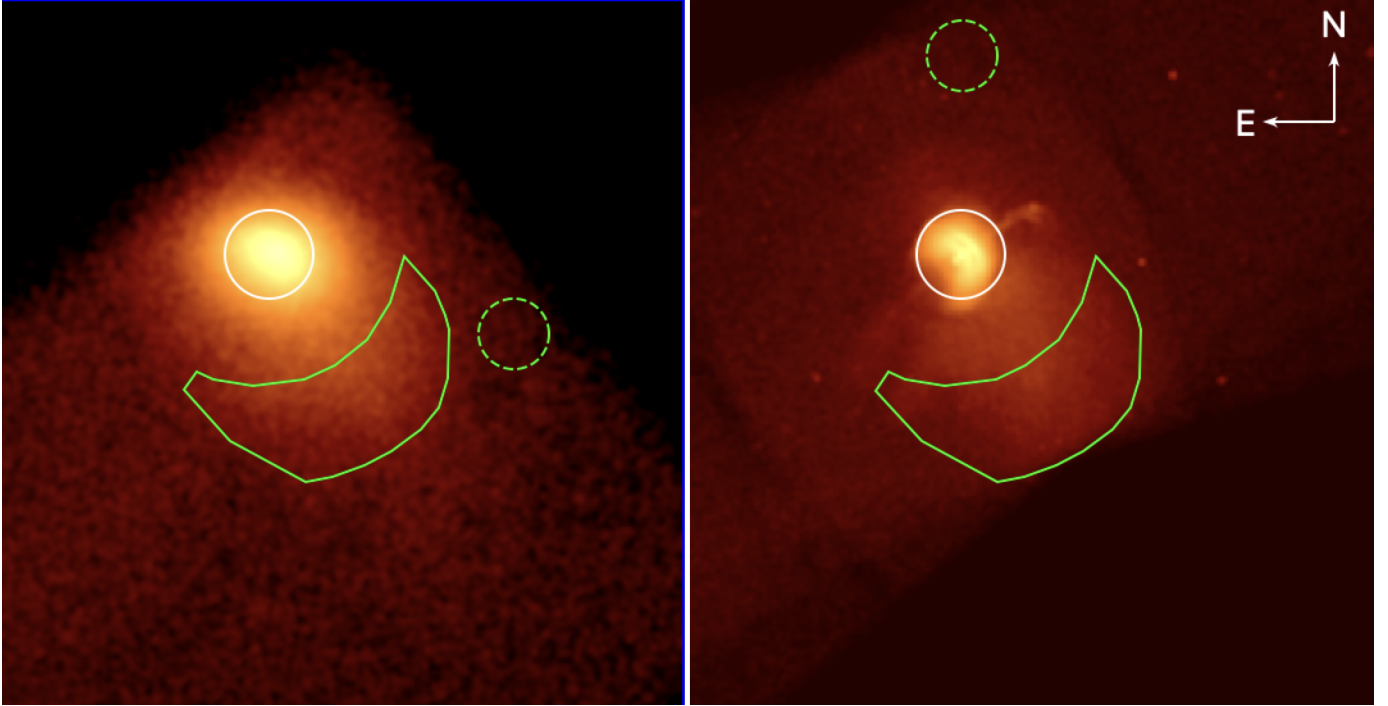


Figure 4. NuSTAR 3-79 keV (left) and CXO 1-8 keV (right) images of the Vela PWN showing the same region of the sky. Both images are binned to $2''$ pixel size and smoothed with $r = 4''$ constant Gaussian kernel. The white ($r = 50''$) and green ($r = 1.2'$) circles show spectral extraction regions for the compact PWN (with exclusion of $r = 3''$ pulsar region; not shown) and SW extension region, respectively. North is up, East is to the left.

of the RXTE PCA and NuSTAR effective area dependencies on energy and the very different spectra of Pk1 and Pk2.

The most intriguing feature of the multiwavelength energy-resolved pulse profiles (shown in, e.g., Figure 4 of Kuiper & Hermsen 2015) is the very different behavior of the Pk1 and Pk2 amplitudes and shapes as a function of energy. It can be summarized concisely

as follows. Pk1 remains narrow and prominent across a very wide energy range from ~ 4 keV to ~ 1 GeV but decays above this energy (see Kuiper & Hermsen 2015 and H. E. S. S. Collaboration et al. 2023). It also disappears (or shifts to a noticeably different phase) in UV and optical (see, e.g., Spolon et al. 2019). On the other hand, Pk2 persists from the optical to the highest gamma-ray energies (~ 100 GeV; H. E. S. S. Collabora-

tion et al. 2018; Lange, et al. in prep.) but becomes weak and broad in hard X-rays. Naively, one may think that the nature of emission (emission mechanism) responsible for Pk2 changes from optical to gamma-rays with the transition to IC happening somewhere in the hard X-ray band. On the other hand, the stability of Pk1 may indicate a single emission mechanism operating in a very broad range of energies. If both peaks are due to emission associated with the particles accelerated in the current sheet outside the light cylinder (as suggested by recent models, e.g., Philippov et al. 2015; Cerutti et al. 2016) then the synchrotron emission from particles with a very broad SED could be the predominant Pk1 emission mechanism. In this case, Pk1 could be associated with positrons propagating outwards in the current sheet located farther away from the pulsar than the Y-point⁹ while Pk2 would be the (synchro-)curvature emission from electrons precipitating towards the star which could be more important at lower energies. The difference in the evolution of Pk1 and Pk2 as a function of energy might also be associated with differences in the direction of motion of the radiating particles (toward vs. away from NS) attributed to the different acceleration history and different emission sites (Y-point vs. current sheet) as proposed by Cerutti et al. (2016). This may also explain the observed significant difference between the slopes of NuSTAR spectra for Pk1 and Pk2. However, a more conclusive answer requires fitting the physical model (such as the one proposed by Cerutti et al. 2016) to multiwavelength phase-resolved spectra (which is beyond the scope of this paper).

Due to the coarse NuSTAR resolution, the pulsar is not resolved well from the surrounding bright compact PWN. Therefore, the pulsed component makes only a small contribution on top of PWN emission in the NuSTAR pulse profile. This only allows us to extract meaningful spectra for the 2 main peaks while using photons from the OP interval as the background. Although the Pk1 spectrum ($\Gamma_1 = 1.10 \pm 0.15$) is substantially harder than the Pk2 spectrum ($\Gamma_2 = 1.62 \pm 0.20$), in qualitative agreement with the Strickman et al. (1999) and Harding et al. (2002) results, the actual best-fit values are different and significantly larger than those reported by Strickman et al. (1999), ($\Gamma_{1,\text{RXTE}} = 0.68 \pm 0.14$ and $\Gamma_{2,\text{RXTE}} = 1.17 \pm 0.12$). While the values reported in Table 2 of Harding et al. (2002) are closer to ours, their Pk1 photon index is still noticeably smaller. Since RXTE PCA is a non-imaging instrument the differences

could be associated with the background treatments in the RXTE data analysis. We note that the new, larger values, are comparable to the photon index values for the hardest elements of the compact bright PWN (see Kargaltsev et al. 2017).

5.2. PWN

Both by fitting just the NuSTAR spectrum and by jointly fitting the NuSTAR and CXO ACIS spectra we find that a single PL cannot adequately describe the spectrum of the compact PWN (extracted from an $r = 50''$ circle centered on the pulsar). At least one spectral break is required¹⁰ to describe the softening of the spectrum with energy. However, the ECPL model provides an even better description of the spectrum at higher energies suggesting a cutoff energy of ~ 50 keV. This indicates that the radiative cooling has a substantial impact on the compact PWN spectrum in agreement with what was observed for this region in the high-resolution CXO spectral maps (restricted to the narrower, 0.5-8 keV, range; Kargaltsev et al. 2017). The overall (spatially-integrated) shape of the spectrum of the compact PWN is crudely consistent with the flat (in F_ν) radio spectrum steepening by ≈ 0.5 (in terms of the spectral index) in the X-ray band and having an exponential cutoff at ~ 50 keV. This is in agreement with the classic picture expected for synchrotron cooling occurring in a stronger magnetic field within the compact PWN (see, e.g., Reynolds 2009). The non-uniformity in the CXO residuals at energies < 3 keV could be attributed to the somewhat varying spectra ($\Gamma = 1.3 - 1.6$) for different parts of the PWN within the $50''$ radius (as can be seen from Figure 1 in Kargaltsev et al. 2017). The SW PWN region spectrum also does not fit a simple PL model and requires either a break near $E_b \approx 3.6$ keV or exponential cutoff with $E_c \approx 50$ keV. Regardless of the model, the slope of the spectrum of the SW PWN region appears to be steeper than that of the same model fitted to the compact PWN spectrum, suggesting that the radiative losses continue impacting particles as they travel away from the pulsar. This behavior is often seen in PWN spectral maps (see, e.g., Guest & Safi-Harb 2020) and is expected in a simple model of radiatively

⁹ See, e.g., Cerutti & Beloborodov 2017, for a modern description of pulsar magnetospheres

¹⁰ While the detailed modeling PWN particle SED evolution is beyond the scope of this paper we note that one should expect the PL to become steeper gradually as a function of distance from the pulsar (an example of calculation in cylindrical geometry is shown in Figure 10 of Chen et al. 2006) if the spectra are extracted from the sufficiently small regions. However, due to the wide PSF or NuSTAR we use large regions and then it is reasonable to expect the gradually softening spectrum can be approximated by a broken PL.

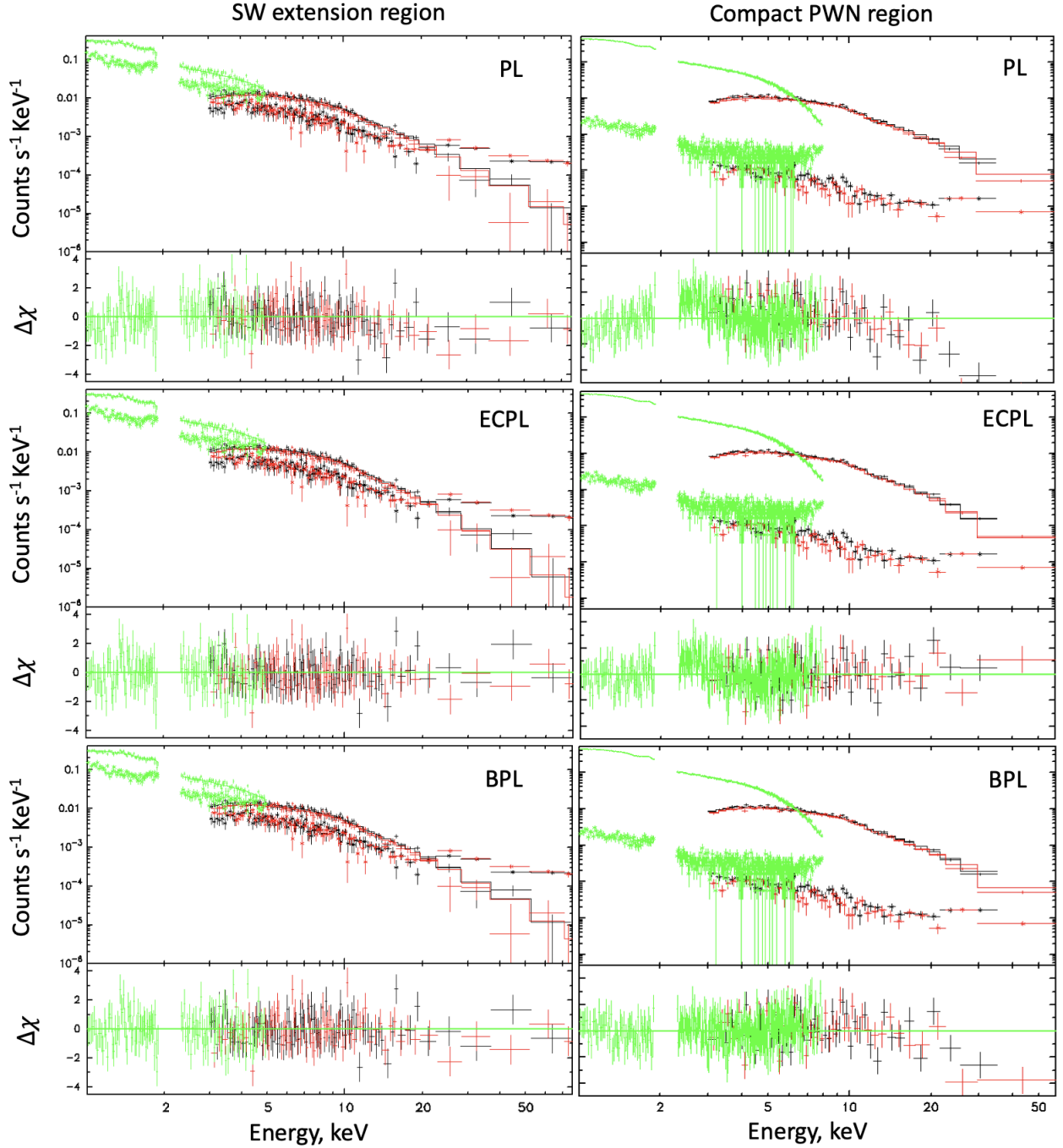


Figure 5. Joint fits to NuSTAR (black and red; for FPMA and FPMB, respectively) and CXO (green) spectra. Background contribution is also shown for each detector/instrument.

cooling wind propagating away from the pulsar (see, e.g., [Chen et al. 2006](#)). However, the spectral steepening is very gradual and the E_c value does not change **much**, indicating that the radiative losses are modest compared to those experienced by particles in the compact PWN region.

The maximum energy available for particle acceleration, $E_{\max} = e(\dot{E}/c)^{1/2} = 4.6$ PeV, which corresponds

to the electron Lorentz factor $\gamma_{\max} = 9 \times 10^9$. Using the standard synchrotron theory [Kargaltsev et al. \(2002\)](#) estimated $B \approx 35 - 50 \mu\text{G}$ just downstream of the termination shock (likely associated with the double arc structure). These estimates should be applicable to the compact PWN region considered in this paper. For these values of magnetic field synchrotron photons energies of $E_{\text{syn}} = 50$ keV imply electron Lorentz factors

$\gamma \approx 3 \times 10^8 (E_{\text{syn}}/50 \text{ keV})^{1/2} (B/40 \text{ } \mu\text{G})^{-1/2}$ which is only about 4% of the potential drop available in the pulsar magnetosphere (for a dipolar field geometry). The corresponding synchrotron cooling time for these electrons is $\tau_c \approx 8(B/40 \text{ } \mu\text{G})^{-3/2} (E_{\text{syn}}/50 \text{ keV})^{-1/2}$ yrs. The inferred maximum Lorentz factors correspond to electron energies of $E_{e,c} \approx 0.15 \text{ PeV}$ is compatible with $E_{e,c} \approx 0.3^{+4}_{-0.2} \text{ PeV}$ obtained by [H. E. S. S. Collaboration et al. \(2019\)](#) from the joint modeling of the TeV and soft X-ray spectra from the larger region including both our compact and SW PWN regions. Although the magnetic field used above in our estimates for the compact PWN is a factor of 3 – 4 higher than that inferred by [H. E. S. S. Collaboration et al. \(2019\)](#), there is no contradiction because the average magnetic field within the much larger volume is likely to be significantly lower than that inside the compact PWN.

6. SUMMARY AND CONCLUSION

The NuSTAR data support a very complex structure of the pulse profile in 3-79 keV with at least 4 peaks per period. By isolating photons with phases belonging to two main peaks (Pk 1 and Pk2) of the pulse profile, we extracted the phase-resolved spectra and fitted them with the PL model finding photon indices of 1.10 ± 0.15 and 1.62 ± 0.20 , respectively. These values are substantially larger than those found earlier from RXTE data.

The fit to NuSTAR and CXO+NuSTAR spectrum for the compact PWN requires a more complex model than a single PL and can be empirically described by a broken PL or, even better, by the exponentially cutoff PL with $E_c \approx 50 \text{ keV}$. The observed softening is likely attributed to the synchrotron cooling in a stronger magnetic field that exists in the compact PWN. The observed energies of synchrotron photons imply that at least 4% of the polar cap potential drop is used to accelerate pulsar wind particles to $\approx 150 \text{ TeV}$ energies, which are in general agreement with those obtained from the joint soft X-ray and TeV spectral modeling by [H. E. S. S. Collaboration et al. \(2019\)](#).

Acknowledgments: We thank Matthew Kerr for providing the Fermi Vela ephemeris. We also thank Matthew Kerr, Paul Ray, and Craig Markwardt for useful conversations regarding pulsar timing. OK is grateful to Sasha Philippov for discussions about pulsar emission models. Finally, we would like to thank the anonymous referee for the careful reading of our paper and insightful comments that helped to improve its quality. Support for this work was provided by the National Aeronautics and Space Administration through the NuSTAR award 80NSSC21K0024. J. H. acknowledges support from NASA under award number 80GSFC21M0002.

REFERENCES

- Arnaud, K. A. 1996, *Astronomical Data Analysis Software and Systems V*, 101, 17
- Bachetti, M., Markwardt, C. B., Grefenstette, B. W., et al. 2021, *ApJ*, 908, 184. doi:10.3847/1538-4357/abd1d610.48550/arXiv.2009.10347
- Bock, D. C.-J., Turtle, A. J., & Green, A. J. 1998, *AJ*, 116, 1886. doi:10.1086/30056310.48550/arXiv.astro-ph/9807125
- Buccheri, R., Bennett, K., Bignami, G. F., et al. 1983, *A&A*, 128, 245
- Cerutti, B. & Beloborodov, A. M. 2017, *SSRv*, 207, 111. doi:10.1007/s11214-016-0315-7
- Cerutti, B., Philippov, A. A., & Spitkovsky, A. 2016, *MNRAS*, 457, 2401. doi:10.1093/mnras/stw124
- Chen, Y., Wang, Q. D., Gotthelf, E. V., et al. 2006, *ApJ*, 651, 237. doi:10.1086/507017
- Dodson, R., Lewis, D., McConnell, D., et al. 2003, *MNRAS*, 343, 116. doi:10.1046/j.1365-8711.2003.06653.x10.48550/arXiv.astro-ph/0302373
- Danilenko, A. A., Zyuzin, D. A., Shibano, Y. A., et al. 2011, *MNRAS*, 415, 867. doi:10.1111/j.1365-2966.2011.18753.x10.48550/arXiv.1103.4871
- Dodson, R., Lewis, D., McConnell, D., et al. 2003, *MNRAS*, 343, 116. doi:10.1046/j.1365-8711.2003.06653.x
- Durant, M., Kargaltsev, O., Pavlov, G. G., et al. 2013, *ApJ*, 763, 72. doi:10.1088/0004-637X/763/2/7210.48550/arXiv.1211.0347
- Espinoza, C. M., Lyne, A. G., & Stappers, B. W. 2017, *MNRAS*, 466, 147. doi:10.1093/mnras/stw3081
- Guest, B. T. & Safi-Harb, S. 2020, *MNRAS*, 498, 821. doi:10.1093/mnras/staa2364
- Harding, A. K., Strickman, M. S., Gwinn, C., et al. 2002, *ApJ*, 576, 376. doi:10.1086/34173210.48550/arXiv.astro-ph/0205183
- Harrison, F. A., Craig, W. W., Christensen, F. E., et al. 2013, *ApJ*, 770, 103. doi:10.1088/0004-637X/770/2/10310.48550/arXiv.1301.7307
- Helfand, D. J., Gotthelf, E. V., & Halpern, J. P. 2001, *ApJ*, 556, 380. doi:10.1086/32153310.48550/arXiv.astro-ph/0007310

- H. E. S. S. Collaboration, Abdalla, H., Aharonian, F., et al. 2018, *A&A*, 620, A66. doi:10.1051/0004-6361/201732153
- H. E. S. S. Collaboration, Abdalla, H., Aharonian, F., et al. 2019, *A&A*, 627, A100. doi:10.1051/0004-6361/201935458
- H. E. S. S. Collaboration, Aharonian, F., Ait Benkhali, F., et al. 2023, *Nature Astronomy*, 7, 1341. doi:10.1038/s41550-023-02052-3
- Kargaltsev, O., Pavlov, G. G., Sanwal, D., et al. 2002, *Neutron Stars in Supernova Remnants*, 271, 181
- Kargaltsev, O. & Pavlov, G. 2004, *Young Neutron Stars and Their Environments*, 218, 195. doi:10.48550/arXiv.astro-ph/0310767
- Kargaltsev, O., Klingler, N., Chastain, S., et al. 2017, *Journal of Physics Conference Series*, 932, 012050. doi:10.1088/1742-6596/932/1/012050
- Kuiper, L. & Hermsen, W. 2015, *MNRAS*, 449, 3827. doi:10.1093/mnras/stv426
- Luo, J., Ransom, S., Demorest, P., et al. 2021, *ApJ*, 911, 45. doi:10.3847/1538-4357/abe62f
- Madsen, K. K., Beardmore, A. P., Forster, K., et al. 2017, *AJ*, 153, 2. doi:10.3847/1538-3881/153/1/2
- Mattana, F., Götz, D., Terrier, R., et al. 2011, *ApJL*, 743, L18. doi:10.1088/2041-8205/743/1/L18
- Pavlov, G. G., Zavlin, V. E., Sanwal, D., et al. 2001, *ApJL*, 552, L129. doi:10.1086/320342
- Pavlov, G. G., Kargaltsev, O. Y., Sanwal, D., et al. 2001, *ApJL*, 554, L189. doi:10.1086/32172110.48550/arXiv.astro-ph/0104264
- Pavlov, G. G., Teter, M. A., Kargaltsev, O., et al. 2003, *ApJ*, 591, 1157. doi:10.1086/37553110.48550/arXiv.astro-ph/0305510
- Philippov, A. A., Spitkovsky, A., & Cerutti, B. 2015, *ApJL*, 801, L19. doi:10.1088/2041-8205/801/1/L19
- Porth, O., Vorster, M. J., Lyutikov, M., et al. 2016, *MNRAS*, 460, 4135. doi:10.1093/mnras/stw1152
- Posselt, B., Pavlov, G. G., Ho, W. C. G., et al. 2024, *arXiv:2407.04337*. doi:10.48550/arXiv.2407.04337
- Reynolds, S. P. 2009, *ApJ*, 703, 662. doi:10.1088/0004-637X/703/1/662
- Romani, R. W., Kargaltsev, O., & Pavlov, G. G. 2005, *ApJ*, 627, 383. doi:10.1086/43026910.48550/arXiv.astro-ph/0503331
- Sanwal, D., Pavlov, G. G., Kargaltsev, O. Y., et al. 2002, *Neutron Stars in Supernova Remnants*, 271, 353. doi:10.1086/200166
- Slane, P., Lovchinsky, I., Kolb, C., et al. 2018, *ApJ*, 865, 86. doi:10.3847/1538-4357/aada12
- Strickman, M. S., Harding, A. K., & de Jager, O. C. 1999, *ApJ*, 524, 373. doi:10.1086/307802
- Spolon, A., Zampieri, L., Burtovoi, A., et al. 2019, *MNRAS*, 482, 175. doi:10.1093/mnras/sty2605
- Wilms, J., Allen, A., & McCray, R. 2000, *ApJ*, 542, 914. doi:10.1086/317016
- Xie, F., Di Marco, A., La Monaca, F., et al. 2022, *Nature*, 612, 658. doi:10.1038/s41586-022-05476-5